JOURNAL OF GEOPHYSICAL RESEARCH, VOL. 97, NO. A11, PAGES 17,005–17,018, NOVEMBER 1, 1992

Interference Patterns in the Spacelab 2 Plasma Wave Data: Oblique Electrostatic Waves Generated by the Electron Beam

WEI FENG, DONALD A. GURNETT, AND IVER H. CAIRNS

Department of Physics and Astronomy, University of Iowa, Iowa City

During the Spacelab 2 mission the University of Iowa's Plasma Diagnostics Package (PDP) explored the plasma environment around the shuttle. Wideband spectrograms of plasma waves were obtained from the PDP at frequencies of 0–30 kHz and at distances up to 400 m from the shuttle. Strong low-frequency (below 10 kHz) electric field noise was observed in the wideband data during two periods in which an electron beam was ejected from the shuttle. This noise shows clear evidence of interference patterns caused by the finite (3.89 m) antenna length. The low-frequency noise was the most dominant type of noise produced by the ejected electron beam. Analysis of antenna interference patterns generated by these waves permits a determination of the wavelength, the direction of propagation, and the location of the source region. The observed waves have a linear dispersion relation very similar to that of ion acoustic waves. The waves are believed to be oblique ion acoustic or high-order ion cyclotron waves generated by a current of ambient electrons returning to the shuttle in response to the ejected electron beam.

1. INTRODUCTION

During the Spacelab 2 flight, a spacecraft called the Plasma Diagnostics Package (PDP) was released from the space shuttle to investigate phenomena associated with the passage of a large vehicle through the ionosphere and the injection of electron beams into the ambient ionosphere. The PDP provided observations in free flight out to a distance of about 400 m from the space shuttle. A Langmuir probe, an ion mass spectrometer, a hot plasma analyzer, a differential ion flux probe, and a plasma wave receiver were among the instruments on board the PDP. For a description of this instrumentation the reader is referred to *Shawhan* [1982]. The PDP was designed and constructed at the University of Iowa and was a reflight of the spacecraft previously flown on the STS 3 flight [*Shawhan et al.*, 1984].

Spacelab 2 was launched into a nearly circular low-inclination orbit with a nominal altitude of about 325 km and an inclination of 49.5°. The PDP was in free flight around the shuttle from 0010 to 0620 UT on August 1, 1985. During this roughly 6-hour interval the shuttle performed two complete fly-arounds of the PDP. These fly-arounds provided measurements both upstream and downstream from the shuttle, and along the magnetic field lines threading the shuttle. In addition to the fly-arounds, a series of wake transits were performed to survey the wake region directly downstream from the shuttle. Among the various investigations performed was a study of the effects produced by a 1-keV electron beam ejected from the shuttle, the so-called Fast Pulse Electron Generator (FPEG) experiment [*Shawhan*, 1982]. The electron beam was operated during two magnetic conjunctions between the shuttle and the PDP (0330–0337 and 0411–0418 UT), and also at other times (0046–0050, 0119–0123, and 0247–0250 UT) when the PDP was not magnetically connected to the shuttle. The FPEG generated a 1-keV electron beam at currents of either 50 mA or 100 mA and had the capability of operating in a pulsed or DC mode. The pulsed emissions could be varied over a wide range of pulse periods, duty cycles, and number of pulses. All free-flyer beam sequences were executed in order to perform a quantitative investigation of electromagnetic radiation and associated plasma disturbances from DC and pulsed electron beams. Artificially generated electron beams such as the FPEG experiment provide a unique means to investigate beam-plasma interactions under relatively controlled conditions. Motivations for such injection experiments include the simulation of natural auroral phenomena and vehicle charging effects, as well as the generation of plasma waves [*Winckler*, 1980; *Bush et al.*, 1987].

The plasma wave receiver on the PDP spacecraft detected intense waves during times when the electron gun was being operated [*Gurnett et al.*, 1986; *Farrell et al.*, 1988; *Gurnett et al.*, 1988; *Frank et al.*, 1989; *Reeves et al.*, 1988, 1990]. *Gurnett et al.* [1986, 1988] and *Farrell et al.* [1988] reported on funnel-shaped whistler mode radiation from electron beams during the 0330–0337 UT magnetic conjunction. *Reeves et al.* [1988, 1990] reported on broadband very low frequency (VLF) electromagnetic wave emissions from both the DC and pulsed modes of operation, as well as narrowband emissions observed during the pulsed beam conjunctions. *Frank et al.* [1989] showed measurements of hot electrons returning from the direction of propagation of the beam during the 0411–0417 UT magnetic conjunction. Large intensifications of broadband waves, especially at very low frequencies, were also observed in association with these returning electrons. All of the above papers concentrated on data from FPEG firings during the two magnetic conjunction events at 0330–0337 UT and 0411–0418 UT.

This paper presents a detailed analysis of so-called "fingerprint" patterns in the electrostatic wave spectra from the wideband receiver, which is part of the PDP plasma wave instrument. In this paper we concentrate exclusively on spin-modulated fingerprint patterns that were associated with electron beam firings. Fingerprint patterns are well known in space plasma physics. They are caused by electrostatic waves with wavelengths short compared to the antenna length [*Temerin*, 1979; *Fuselier and Gurnett*, 1984; *Gallagher*, 1985]. A theoretical review of antenna interference effects is presented in section 2. The observations are

Paper number 92JA00989.
0148-0227/92/92JA-00989$05.00

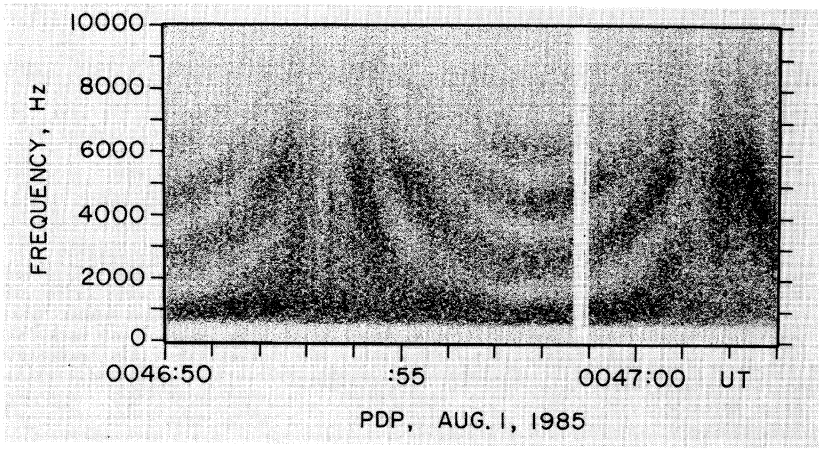

Fig. 1. An example of an interference pattern observed in the 0- to 10-kHz electric field wideband spectrum. This is a frequency-time spectrum obtained over a 13-s interval (0046:50–0047:03 UT) on August 1, 1985.

presented in section 3. Methods for determining the wave frequency, the propagation directions, and the dispersion relation from these interference patterns are described in section 4. It is concluded that the low-frequency electrostatic waves are most likely obliquely propagating ion acoustic or high-order ion cyclotron waves. In section 5 the source location of these waves and the wave vector distribution required for formation of an antenna interference pattern are discussed. The results from a linear growth rate analysis of ion acoustic–like instabilities are presented in section 6.

2. Antenna Interference Effects

Interference patterns can be used to determine the wavelength, the direction of propagation, the Doppler shift, and the rest frame frequency of short-wavelength waves. An example of an interference pattern observed in the PDP data is shown in Figure 1. Figure 1 shows a frequency-time spectrum obtained over a 13-s interval (0046:50–0047:03 UT) on August 1, 1985. The "fingerprint" pattern caused by the rotation of the antenna in the wave field is clearly evident.

To help understand these interference effects, it is useful to review the response of an electric dipole antenna to an electrostatic wave. The following is a development similar to the theory introduced by *Temerin* [1979] and *Gallagher* [1985]. The coordinate system used for this study is the local vertical/local horizontal (LVLH) reference system commonly used in the analysis of data from the space shuttle. The Z axis in this reference system lies along the geocentric radius vector to the spacecraft and is positive toward the center of the Earth. The X axis lies in the orbital plane and is positive in the direction of spacecraft motion. The Y axis is normal to the orbital plane and completes the right-handed orthogonal coordinate system. The geometry of this coordinate system is illustrated in Figure 2. The potential $\Delta\Phi$ of an electrostatic wave between two points in space separated by a vector $d\mathbf{r}$ is given by

$$\Delta\Phi = -\mathbf{E} \cdot d\mathbf{r}, \tag{1}$$

where $\mathbf{E}$ is the electric field. During the free flight the spin axis of the PDP is oriented perpendicular to the orbital plane. Therefore we assume that the electric antenna is rotating in the X-Z plane. The electric field can be given by

$$\mathbf{E} = (E_{xz}\hat{\rho} + E_y\hat{y})e^{i(\mathbf{k}\cdot\mathbf{r}-\omega t)},$$

where $\hat{\rho}$ is a unit vector and E_{xz} is the magnitude of $\mathbf{E}$ projected onto the X-Z plane. The PDP electric field antenna consists of two spherical probes separated by a distance of 3.89 m. The antenna is presumed to respond to the potential difference in the plasma between the two probes. We define $\mathbf{l}$ to be the vector along the antenna axis and k_{xz} to be the magnitude of $\mathbf{k}$ projected onto the X-Z plane. Therefore substituting $\mathbf{l}$ for $\mathbf{r}$, we have $d\mathbf{r} = d\mathbf{l}$ and $\mathbf{k} \cdot \mathbf{r} = k_{xz}l \cos\phi$, where ϕ is the angle between $\hat{\rho}$ and $\mathbf{l}$. Integrating equation (1) between two probes located at $-l/2$ and $l/2$ gives

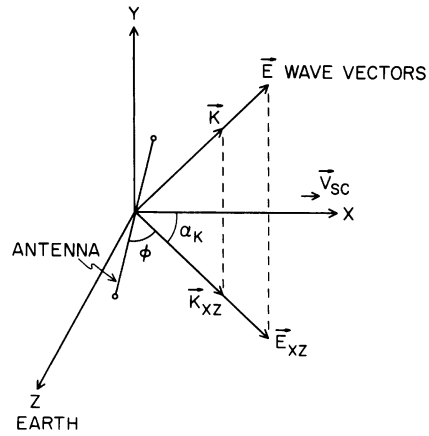

Fig. 2. The PDP's antenna position in the LVLH coordinate system. The Z axis in the LVLH system lies along the geocentric radius vector to the spacecraft and is positive toward the center of the Earth. The X axis lies in the orbital plane and is positive in the direction of spacecraft motion. The Y axis is normal to the orbital plane and completes the right-handed orthogonal system. The electric antenna is rotating in the X-Z plane.

$$\Delta\Phi = \frac{-2(E_{xz}\cos\phi)\sin[k_{xz}(l/2)\cos\phi]e^{-i\omega t}}{k_{xz}\cos\phi}. \quad (2)$$

The measured voltage, V_m, is the root-mean-square of the average potential difference between the spheres, which from equation (2) is given by

$$V_m = \frac{[\Delta\Phi\Delta\Phi^*]^{1/2}}{2} = E_{xz}l|\cos\phi|\left|\frac{\sin(x\cos\phi)}{x\cos\phi}\right| \quad (3)$$

where $x = k_{xz}l/2$. For waves with wavelength $\lambda \gg l$ the $|\sin(x\cos\phi)/x\cos\phi|$ term in equation (3) approaches unity, and the usual cosine spin modulation in the power spectrum is obtained. If $\lambda \sim l$, then the $|\sin(x\cos\phi)/x\cos\phi|$ term produces a characteristic spin-modulated interference pattern that can be observed in the wideband data. To understand this term more thoroughly, it is useful to determine the conditions for minima and maxima in the measured voltage. One condition for minima in the measured voltage occurs when $\sin(x\cos\phi)$ is zero. This condition can be expressed as

$$\frac{k_{xz}l\cos\phi}{2} = m\frac{\pi}{2} \quad (4)$$

where m is an even integer ($m = 2, 4, 6, \cdots$). The nulls indicated by equation (4) can be used to determine the components of the wave vector in the antenna spin plane (X-Z plane). The characteristic shape of a typical interference pattern can be explained by rewriting (4) in the following form,

$$l\cos\phi = \frac{m}{2}\lambda, \quad (5)$$

where λ is the wavelength projected onto the X-Z plane ($k_{xz} = 2\pi/\lambda$). For a fixed antenna position, equation (5) shows that the condition for a minimum ($V_m = 0$) is met when an integral number of wavelengths is projected onto the antenna.

To analyze the dispersion relation of the waves, it is useful to compute the frequency in the rest frame of the plasma. The rest frame frequency can be obtained by subtracting the Doppler shift from the frequency measured in the spacecraft frame of reference. The relevant equation is

$$\omega' = \omega_0 - \mathbf{k}\cdot\mathbf{V}_{sc}, \quad (6)$$

where ω' is the frequency measured in the spacecraft frame of reference, ω_0 is the frequency in the plasma rest frame, and $\mathbf{V}_{sc}$ is the velocity of the spacecraft relative to the plasma. Since the spacecraft velocity vector is directed along the X axis, this equation simplifies to

$$\omega' = \omega_0 - k_x V_{sc} = \omega_0 - k_{xz}V_{sc}\cos\alpha_{k0}, \quad (7)$$

where α_{k0} is the angle between the spacecraft velocity vector and the projection ($\mathbf{k}_{xz}$) of the wave vector onto the X-Z plane.

A null at a certain frequency in the wideband data corresponds to a projected wave vector with zero potential. As the antenna rotates, the angle ϕ between the projected wave vector and the antenna varies. As this angle approaches $\pm\pi/2$, larger and larger projected wave vectors are required to meet the null condition. The null therefore moves to higher frequencies as $\phi \to \pm\pi/2$, thereby forming the walls of the pattern's U shape. The pattern repeats every one-half spacecraft rotation. The center of the U-shaped interference pattern thus gives the direction of the wave vector projected onto the spin plane of the antenna.

Maxima in the antenna voltage can also be used to determine the direction and magnitude of the wave vector projected onto the spin plane. Maxima occur when $\tan(x\cos\phi) = (x\cos\phi)$ is met or approximately when

$$\frac{k_{xz}l\cos\phi}{2} = m\frac{\pi}{2} \quad (8)$$

where $m = 0, 2.86, 4.92, 6.94, \cdots$. Note that at $m = 0$ the voltage has its largest maximum. In addition, as may be shown using the turning points of equation (3), the maximum expected at $m \simeq 1$ disappears due to the strength of the $m = 0$ maximum.

It is important to realize that the analysis of the interference pattern does not give any information about the component of the wave vector perpendicular to the spin plane. This information is lost when the dot product $\mathbf{E}\cdot d\mathbf{r}$ is taken to find the potential. This missing piece of information must be carefully considered when estimating wavelengths and determining the direction of propagation. Fortunately, for the PDP data the perpendicular component of the wave vector does not enter into the calculation of the Doppler shift because the spacecraft spin axis is oriented perpendicular to the plasma flow velocity so that $k_y V_{scy} = 0$.

To interpret the wideband spectrum, the measured voltage spectral density must be related to the electric field spectral density of the wave. From the above discussion one can see that the voltage spectral density is given by

$$P(k_{xz}, \phi) = \frac{(V_m)^2}{\Delta f} = \frac{E_0^2(k_{xz})l^2}{\Delta f}\frac{\sin^2(x\cos\phi)}{x^2}, \quad (9)$$

where E_0 is the wave electric field strength and Δf is the measurement bandwidth. The frequency ω of the wideband data is related to the wave number k_{xz} through equation (7). In reality the waves propagate over a range of angles α_k, centered at α_{k0}. Integrated over all propagating angles, assuming an angular distribution $F(\alpha_k)$, the measured spectral density is given by

$$P_{\text{mea}}(k_{xz}, \phi) = \left(\frac{V_m^2}{\Delta f}\right)_{\text{mea}} = \frac{E_0^2(k_{xz})}{\Delta f}l^2 \cdot \int F(\alpha_k)\frac{\sin^2\{x(\alpha_k)\cos[\phi(\alpha_k)]\}}{x^2(\alpha_k)}d\alpha_k. \quad (10)$$

The electric field spectral density, corrected for the antenna response, is then given by

$$\frac{E_0^2(k_{xz})}{\Delta f} = P_{\text{mea}}(k_{xz}, \phi) \cdot \left\{l^2\int F(\alpha_k)\frac{\sin^2\{x(\alpha_k)\cos[\phi(\alpha_k)]\}}{x^2(\alpha_k)}d\alpha_k\right\}^{-1}. \quad (11)$$

Equation (10) will be used to numerically stimulate various interference patterns in section 5. Using equation (11), the

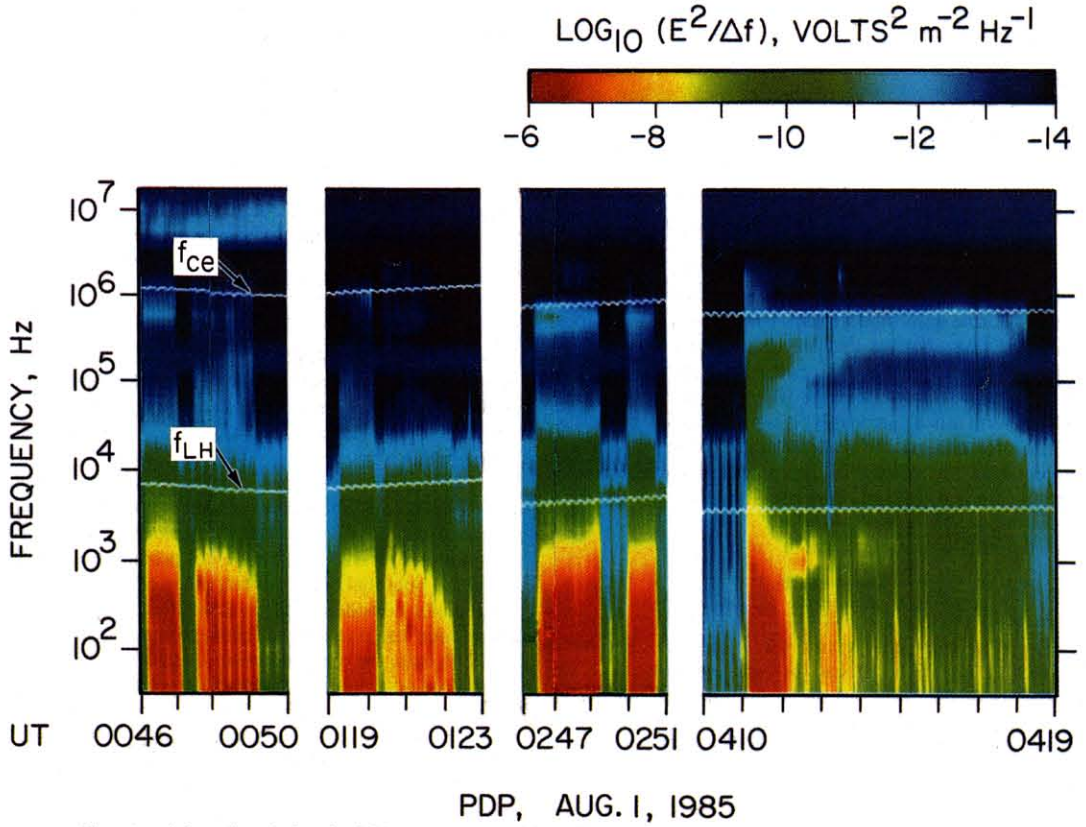

Plate 1. A broadband electric field spectrogram with Helios and MFR data for the time periods 0046–0047, 0119–0213, 0247–0251, and 0411–0419 UT. The electric field spectral density, $E/\Delta f$ where Δf is the bandwidth of the filter channel, is color-coded with blue being the least intense and red being the most intense. The white curves labeled f_{ce} and f_{LH} are the electron cyclotron and lower hybrid frequencies, respectively. The intense (red and yellow color) waves below about 5 kHz are the waves associated with the injected FPEG electron beams. In each of the four events shown here, complete or partial antenna interference patterns are found in the 0- to 10-kHz electric field wideband data.

true density spectrum of the waves as a function of wave number k_{xz} (or frequency) can therefore be deduced from the wideband interference patterns.

3. Observations

During the 6 hours of free flight, the PDP was spin stabilized with a rotation period of 13.6 s. In addition to the wideband receiver, the PDP plasma wave instrument includes an array of band-pass filters. The filter array includes the IMP/Helios instrument, which consists of 16 channels with 10% bandwidths in the frequency range from 31 Hz to 178 kHz, and the medium-frequency receiver (MFR), which consists of eight channels with 10% bandwidths in the frequency range from 316 kHz to 17.8 MHz. The electron gun was operated in various modes during the following time periods: 0046–0050, 0119–0123, 0247–0251, 0330–0337, and 0411–0418 UT. Intense low-frequency waves accompany each of these electron gun firings, in all cases being confined to the times of the gun firings, within the time resolution of the wave instruments (1.6 s). Plate 1 shows a broadband electric field spectrogram from the Helios and MFR data for the time periods 0046–0050, 0119–0123, 0247–0251, and 0411–0419 UT. The electric field spectral density, $E^2/\Delta f$ where Δf is the bandwidth of the filter channel, is color-coded with blue being the least intense and red being the most intense. The white curves labeled f_{ce} and f_{LH} are the electron cyclotron and lower hybrid frequencies, respectively. The intense (red and yellow color) waves below about 5 kHz are the waves associated with the injected FPEG electron beam. A snapshot of the electric field density spectrum at 0046–0047 UT is given in Figure 3. The electric field spectral density of the low-frequency waves (below 10 kHz) is 1–4 orders of magnitude larger than the spectral density at higher frequencies. Accordingly, the dominant waves produced by the electron beam ejections are very low frequency waves. Note that the frequencies were measured in the frame of the PDP. As we show in the following analysis, the wavelengths are so short (approximately a few meters) that the frequency observed in the spacecraft rest frame is mainly determined by the Doppler shift. In each of the four events shown in Plate 1, complete or partial antenna interference patterns are found in the 0- to 10-kHz electric field wideband data. Although similarly intense low-frequency waves are visible in the Helios/MFR data for the

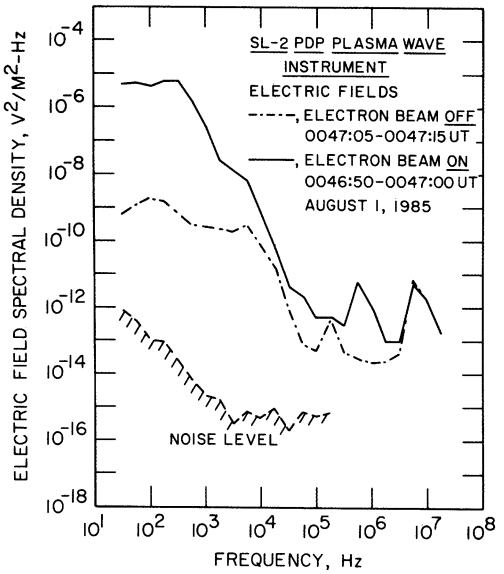

Fig. 3. The electric field spectral density as a function of the frequency during the 0046–0047 UT event and the comparison with the electron beam off and the background noise level. As shown when the electron beam is on, the spectral density increases significantly in the very low frequency region and near the electron plasma frequency region.

0330–0337 UT event (see Plate 1 of *Farrell et al.* [1988]), no interference pattern was found in the corresponding 0- to 10-kHz wideband data.

The wideband receiver provides measurements in four frequency bands, with frequency limits of 40 Hz to 1 kHz, 400 Hz to 10 kHz, 10 kHz to 20 kHz, and 20 kHz to 30 kHz. The wideband receiver was connected alternately to the 3.89-m double-sphere electric antenna and to a 16-inch 10,000-turn magnetic field search coil. Every fourth magnetic antenna cycle was replaced by a Langmuir probe period. This antenna switching pattern is shown in Figure 4. In addition, the upper three frequency bands are subjected to an additional switching pattern. In both the electric and magnetic antenna periods the 0- to 10-kHz band was measured for 25.6 s, and the 20- to 10-kHz (with inverted frequency response) and 20- to 30-kHz bands were measured for 12.8 s each, to give a total period of 51.2 s. The antenna switching pattern and the frequency band switching pattern account for the apparent gaps and discontinuities in the wideband data as well as the lack of simultaneous electric and magnetic field data. For the wideband data the total output signal strength was kept within closely controlled limits by an automatic gain control (AGC). The absolute intensity of the waves therefore cannot be obtained directly from the wideband data. In this study, we shall mainly use wideband electric field measurements in the 0- to 10-kHz range.

All of the antenna interference patterns associated with electron beam ejections were observed in the 0- to 10-kHz electric field spectrum. No interference patterns were observed in the 10- to 20-kHz or 20- to 30-kHz frequency ranges. The absence of interference patterns in the upper two frequency bands is apparently due to the rapid decrease in the wave intensity with increasing frequency. During the 0046–0047 UT and 0247–0250 UT events, very clear interference patterns were obtained in the 0- to 10-kHz data. The corresponding spectrograms are shown in Figures 1 and 5. The antenna interference patterns correspond exactly with the time periods of operation of the FPEG gun. During the 0046–0047 UT event the electron gun operated in the DC mode from 0046:11 UT to 0047:05 UT. Wideband electric field data in the 0- to 10-kHz frequency range are available from 0046:49 UT to 0047:15 UT. An interference pattern started at the beginning of this interval (0046:50 UT) and stopped in the middle of the next period (0047:05 UT). The termination of the interference pattern corresponds exactly with the termination of the gun firing (DC mode). In the 0247–0250 UT FPEG event, the electron gun fired in the DC mode from 0247:29 UT to 0249:16 UT, followed by a break from 0249:16 UT to 0249:59 UT, and on again until 0250:45 UT. The 0- to 10-kHz electric field spectra were obtained for two time intervals. The first was from 0248:01 UT to 0248:27 UT, during which a clear interference pattern was visible

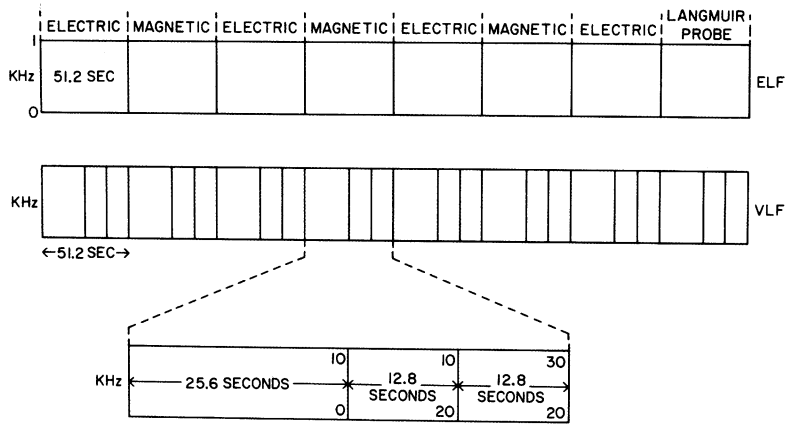

Fig. 4. One complete antenna sequence for both the PDP ELF and VLF wideband data.

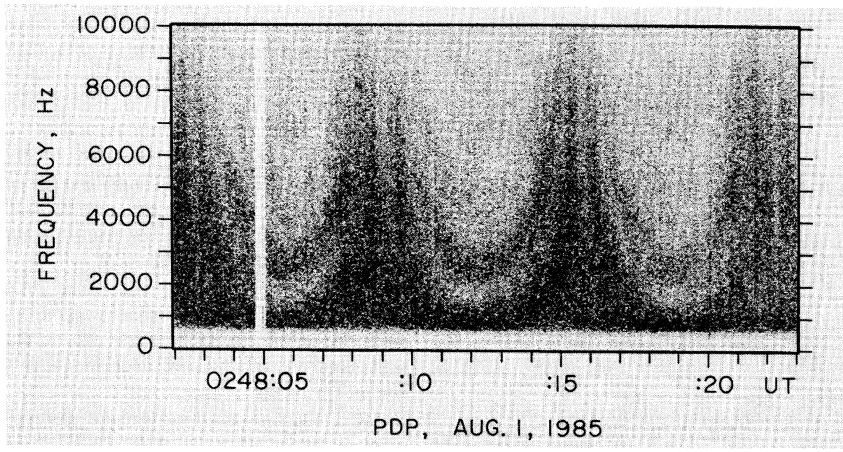

Fig. 5. Another example of an interference pattern observed in the 0- to 10-kHz electric field wideband spectrum. This is a frequency-time spectrum obtained over a 21-s interval (0248:02–0248:23 UT) on August 1, 1985.

over the entire time period. The second was from 0249:43 to 0250:09 UT, during which an interference pattern started in the middle (0249:59 UT) and stopped at the end (0250:09 UT).

During the 0411–0418 UT event the electron gun was pulsed at 1.22 kHz with a 50-50 duty cycle. During this period, 0- to 10-kHz electric field wideband spectra were measured 5 times, including the period from 0411 to 0412 UT shown in Figure 6. The influence of the antenna rotation can be seen, although the interference patterns are unclear and only partially formed. The interference patterns are only observed in this period (0411–0412 UT). During the period from 0119 to 0120 UT, while the FPEG was operating in the DC mode, a poorly resolved and partial interference pattern was observed in the 0- to 10-kHz range.

In order to confirm that the observed waves are electrostatic, a comparison was made between the electric field and magnetic field data. The wideband receiver was alternately connected to the electric antenna, the magnetic search coil, and less frequently to the Langmuir probe. Only a few frames of 0- to 10-kHz magnetic field data were obtained during period when the interference patterns were observed in the electric field data. No wideband 0- to 10-kHz magnetic data were obtained during the 0046–0047 UT event. The 0247–0250 UT event included only one period of 0- to 10-kHz magnetic data starting at 0250:35 UT. These magnetic field spectrograms show that a background level of electromagnetic whistler mode radiation was present at a frequency of about 5 kHz from 0240 UT to 0258 UT. This whistler mode radiation occurred both before and after the FPEG event and was clearly evident in both the electric and the magnetic wideband data. During the period when the electron gun was firing and 0- to 10-kHz electric field data were available, the 5-kHz whistler radiation was not visible in the electric field wideband spectrum but remained visible in the magnetic field wideband data. Since operation of the AGC permits only the strongest waves to be recorded, apparently the beam-associated electrostatic waves are much stronger than the background whistler mode radiation. No interference patterns were observed in the magnetic field data. Since the whistler mode waves are the dominant waves in the magnetic field data during the FPEG event, the beam-associated

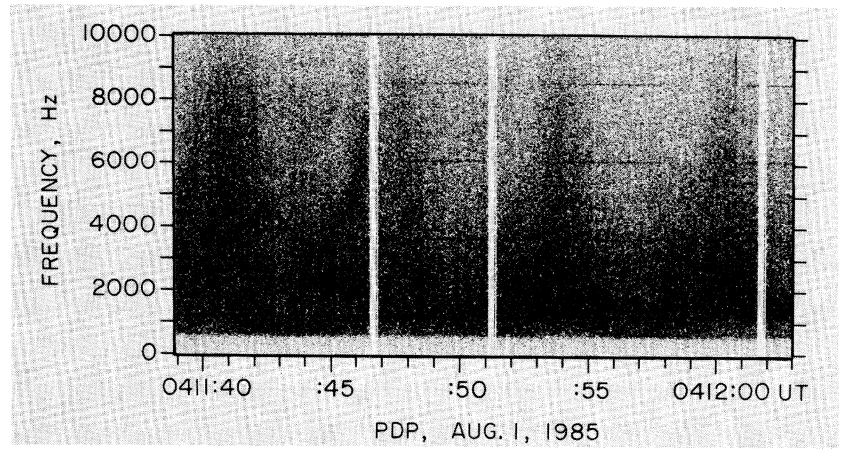

Fig. 6. An example of a partially formed interference pattern observed in the 0- to 10-kHz electric field wideband spectrum. This is a frequency-time spectrum obtained over a 24-s interval (0411:39–0412:03 UT) on August 1, 1985.

TABLE 1. FPEG Experiments During the PDP Free Flight

Beam Time, UT	Beam Type	Fingerprint	X, m	Y, m	Z, m	R, m
0046:11–0047:05	DC	clear	−95	−4	−5	93
0047:31–0049:16	ELF1	none	−96	−4	−4	89
0119:23–0120:17	DC	unclear	−92	−2	−1	92
0120:33–0123:18	ELF1	none	−96	0	−7	98
0247:29–0249:16	DC	clear	−209	−25	−108	161
0249:59–0250:53	DC	clear	−215	−22	−95	172
0330:12–0337:22	DC	none	55	−92	189	15–30
0411:13–0417:24	1.22 kHz	unclear	−144	−53	−156	2–30

waves must be primarily electrostatic. During the 0411–0418 UT event, 0- to 10-kHz magnetic wideband data were obtained 5 times, and only the electron gun AC modulation frequency (1.22 kHz) and its harmonic were observed. In the 0411–0412 UT event as well, the waves forming the observed interference pattern are also electrostatic and are similar to the waves observed in the 0046–0047 UT and 0247–0250 UT events.

During the 0330–0337 UT event the electron gun fired in the DC mode. No interference patterns were observed in the 0- to 10-kHz range, although strong electric field signals associated with the electron beam are present during this period. Since the electron gun operated over a long interval, ~7 min, many 0- to 10-kHz magnetic field spectra were obtained. By comparing the magnetic field wideband data with the electric field data, it is clear that the electric signals are caused by electromagnetic waves. During the 0047–0049 UT and 0120–0122 UT events the electron gun was being operated in the ELF1 mode, in which the electron gun was modulated at various frequencies from 9.54 Hz to 610 Hz. The electric and magnetic field spectrum during this period is dominated by signals that are generated by a beat between the electron gun pulsing and the repetition rate of wideband spectrum analysis. Apparently these signals are due to electromagnetic whistler mode noise. No interference patterns were observed during these periods. The electron gun also operated at several other times (0228–0236 UT and 0338–0400 UT) in the ELF1 mode and the VLF1 mode. While the PDP was on the upstream side of the shuttle, the electron gun was modulated in these modes at various frequencies in the VLF range. No interference patterns or intense electric field noise were observed in the magnetic field data during any of these time periods.

During the 0330–0337 UT and 0411–0418 UT events the PDP passed near the magnetic conjunction point with the shuttle. The magnetic conjunctions occurred at 0333 UT and 0411 UT, respectively. During the 0046–0047, 0119–0120, and 0248–0250 UT events the PDP was not magnetically connected to the shuttle. The perpendicular distances between the PDP and the magnetic conjunction field line were 93, 92, and 170 m, respectively. During the 0330–0337 UT event, when no interference patterns were observed, the PDP was on the upstream side of the shuttle most of the time. During the 0411–0418 UT event, when interference patterns were observed, the PDP was on the downstream side of the shuttle. Table 1 summarizes the characteristics of the electron gun operation during periods when strong levels of low-frequency (≤5 kHz) waves were observed and gives the characteristics of the interference patterns observed and the positions of the PDP relative to the shuttle. The coordinates X, Y, and Z are the PDP position in the LVLH coordinate system centered at the shuttle. The distance R is the perpendicular distance from the PDP to the magnetic field line connected to the shuttle.

4. ANALYSIS

From the interference patterns in Figures 1 and 5 the time when the nulls go to infinite frequency can be precisely determined. From equation (5) it can be seen that this condition occurs at $\phi = \pm\pi/2$, when the antenna is perpendicular to $\mathbf{k}_{xz}$, the component of $\mathbf{k}$ in the X-Z plane. From the antenna position at these times the angle between the projections of $\mathbf{V}_{sc}$ and $\mathbf{k}$ onto the X-Z plane can be determined. This angle is either α or $\alpha + \pi$ with $\alpha < 90°$. The first solution, α, corresponds to a negative Doppler shift with the wave propagating in the upstream direction, and the second solution, $\alpha + \pi$, corresponds to a positive Doppler shift, with the wave propagating in the downstream direction. The Doppler term is the dominant term. By comparing the Doppler term $k_{xz}V_{sc}\cos\alpha_k$ with the measured frequency, the sign of the Doppler term can be determined, and therefore the direction of the wave vector $\mathbf{k}$ in the X-Z plane can be uniquely determined. The angle between the wave vector $\mathbf{k}_{xz}$ and $\mathbf{V}_{sc}$ is 150° for the 0046–0047 UT event and 18° for the 0247–0250 UT event, with ±2° error.

In the plasma rest frame the shuttle and the PDP move with speeds of 7.4 km s^{-1}. These speeds are much larger than the speed of the PDP relative to the shuttle (≤1 m s^{-1}), thereby permitting the PDP's velocity relative to the shuttle to be neglected when computing the Doppler shift. Since we know the angle between $\mathbf{V}_{sc}$ and $\mathbf{k}$ in the X-Z plane, we can calculate the Doppler shift term exactly. Subtracting the Doppler term from the measured frequencies at the nulls and maxima, the dispersion relation for $k_y = 0$ can be determined since $\omega_0 = \omega' + \mathbf{k}\cdot\mathbf{V}_{sc}$. For our cases the Doppler shift term is the dominant term, but since we can calculate it precisely, we can obtain valuable constraints on the dispersion relation in the two-dimensional X-Z plane.

Using the method described above, constraints on the dispersion relation of the waves associated with the electron beam in the 0046–0047 UT and 0247–0250 UT events have been determined. In order to determine the frequency of nulls or maxima, we integrate over a fixed-time interval centered on the symmetry axis of the interference pattern. For example, in Figure 1 a symmetry axis occurs near 0046:58 UT. A least squares fit is used to determine the frequency position of each null and maximum as shown in Figure 7. The corresponding wave vector component in the X-Z plane, k_{xz}, for each null and maximum on the symmetry

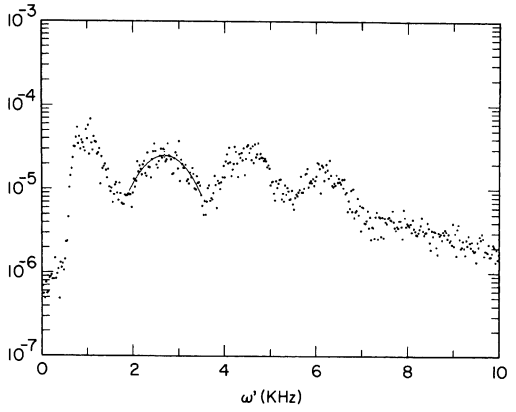

Fig. 7. A snapshot electric field power spectrum obtained at 0046:57.6–0046:58.0 UT. Then a least squares fit is used to determine the maxima and null position of the interference pattern for the 0046–0047 UT event.

axis of the interference pattern can be determined from equations (4) and (8). The Doppler shift and the rest frame frequency are then calculated exactly for each null and maximum, thereby leading to the dispersion relation shown in Figure 8. As shown in Figure 8, the results for different integrating time intervals are very consistent. Noting that a very concentrated angular spectrum of waves is necessary for producing an interference pattern, we may argue that the fully three-dimensional dispersion relation should be very similar to Figure 8 with k_{xz} replaced by k. We note that in this case the Doppler shift term $|\mathbf{k} \cdot (-\mathbf{V}_{sc})|$ is smaller than the observed frequency, implying that the wave vector $\mathbf{k}_{xz}$ has a component directed downstream of the shuttle. For the other event at 0247–0250 UT we find that the absolute value of the Doppler shift term $|\mathbf{k} \cdot (-\mathbf{V}_{sc})|$ is larger than the measured frequency ω'. This means that the waves are directed in the upstream direction for this event. The PDP is further away from the shuttle during this event (~210 m) than during the 0046–0047 UT event (~95 m), and the wave levels are sufficiently low that only one maximum and one

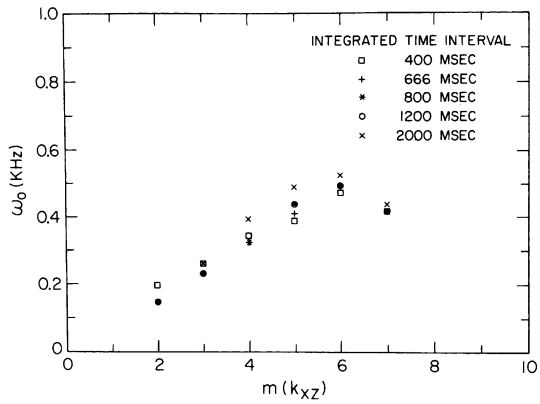

Fig. 8. The dispersion relation of the electrostatic low-frequency waves in the two-dimensional X-Z plane for the 0046–0047 UT event; ω_0 is the wave frequencies in the plasma rest frame.

null position can be clearly identified. The frequency in the plasma rest frame also increases with k_{xz} in the same frequency range as for the 0046–0047 UT event. In summary, the interference patterns for both events are consistent with the waves having rest frame frequencies less than 600 Hz and having an approximately linear dispersion relation. The last point in Figure 8 does deviate from the linear dispersion relationship, possibly because of the poor signal to noise ratio at high frequencies. This point is discussed later in the power spectrum analysis. From the two-dimensional linear dispersion relation in Figure 8 the phase speed of the beam-associated waves can be estimated. Since the phase speed $V_s = \omega/k \leq \omega/k_{xz}$, we conclude that the phase speed of the waves must be less than 700 m s^{-1}.

The plasma in the vicinity of the space shuttle is primarily composed of electrons and oxygen ions from the ionosphere and of water ions formed by charge exchange from water outgassed by the shuttle [*Narcisi et al.*, 1983; *Paterson and Frank*, 1989]. Wherever confidence may be attached to the fitting routine, the data from the retarding potential analyzer on the PDP spacecraft [*Reasoner et al.*, 1986] imply an O^+ temperature of approximately 1000 K (Reasoner, personal communication, 1989). Electron temperatures of 2000–2500 K are often quoted for the Spacelab 2 mission [*Murphy et al.*, 1989; *Tribble et al.*, 1989]. Day-night variations and shuttle water effects imply that factor of 2 variations in electron temperature can occur [*Siskind et al.*, 1984; *Murphy et al.*, 1989; *Tribble et al.*, 1989; *Pickett et al.*, 1989]. For the 0046–0047 UT FPEG event, the only one for which Langmuir probe data are available, $T_e \simeq 2500$ K (J. S. Pickett, personal communication, 1990). This result could, however, be affected by the electron gun firing. We therefore take $T_e = 2000$ K. Water ion temperatures have not been measured. We therefore take $T_{H_2O^+} \sim 300$ K. The thermal speeds of the electrons, oxygen ions, and water ions are then approximately 1.7×10^5, 720, and 370 m s^{-1}, respectively. The phase speed of ion acoustic waves in an unmagnetized plasma is

$$V_s = \left[\frac{k_B(T_e + 3T_i)}{M_i}\right]^{1/2}. \tag{12}$$

For the above electron/oxygen plasma, $V_s \sim 1500$ m s^{-1}. Then, comparing the measured phase speed of the waves with these thermal speeds and the unmagnetized ion acoustic speed, we conclude that the observed waves have phase speeds of the order of the oxygen ion thermal speed and one-half the ion acoustic speed. Given the uncertainties involved, ion acoustic waves are a reasonable possibility. The angle between the measured wave vector $\mathbf{k}_{xz}$ and the magnetic field vector $\mathbf{B}_{xz}$ in the two-dimensional X-Z plane is about 95° for both the 0046–0047 UT event and the 0248–0250 UT event. The true angle between $\mathbf{k}$ and $\mathbf{B}$ in three dimensions should also remain large. These waves therefore propagate at a large angle relative to the magnetic field. Qualitatively the phase speed and direction of propagation suggest that the waves are oblique ion acoustic–like waves.

The true power spectrum as a function of k_{xz} can be determined by eliminating the antenna interference effect using equation (11). The results of such a procedure are shown in Figure 9 for the 0046–0047 UT event. A snapshot spectrum covering the period from 0046:57.6–0046:58.2 UT

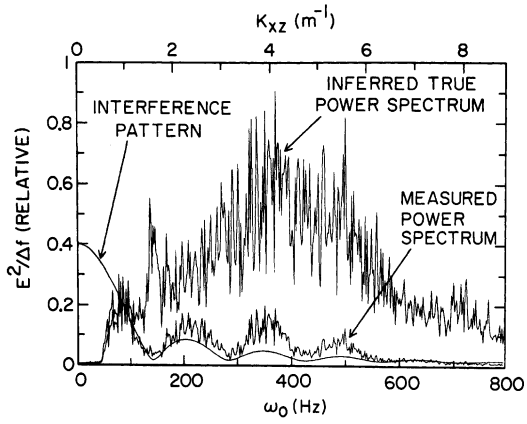

Fig. 9. Inferred true power density spectrum obtained from the measured power spectrum by eliminating the antenna interference effect.

is used. The angular distribution of the waves $F(\alpha_k)$ is assumed to be a Gaussian distribution with a standard deviation of 4°. A standard deviation of 4° is chosen in order to get a smooth fit for the entire power spectrum. The standard deviation is also consistent with the conclusion in the next section that the range of the wave propagation angles is less than 10°. Accordingly, the rapid decrease in intensity for the measured spectrum is mostly due to overlaying by the interference pattern. The true power spectrum initially increases with increasing frequency, reaches a maximum at around 4–5 kHz, and then decreases rapidly. The last point on the two-dimensional dispersion relation in Figure 8 is below the linear line and is due to the decrease in the true power spectrum. Although the waves must propagate in a very concentrated range of angles, they evidently have a broad range of wave numbers.

5. Source Location and Wave Vector Direction

When an electron beam is injected into a homogeneous plasma, a returning background electron flux is required to balance the electron beam current. This elementary notion has been confirmed in a series of plasma simulations performed by *Okuda et al.* [1987], *Okuda and Ashour-Abdalla* [1988, 1990], *Winglee and Pritchett* [1988], and *Pritchett* [1990, and references therein]. The returning electron flux has a net drift relative to the background ions, so that ion acoustic waves can be generated by the return current. Ion acoustic waves can also be produced directly by the electron beam, for instance, by the Buneman instability [*Buneman*, 1958] or as the decay products of beam-driven Langmuir waves. The observed time correlation between continuous operation of the FPEG experiment and the observed ion acoustic–like waves implies that the ion acoustic–like waves are generated either directly by the beam electrons or by electrons carrying a return current back to the shuttle. During both the 0046–0047 UT and 0247–0250 UT events the waves propagate obliquely to the magnetic field, and the component of the wave vector direction along the magnetic field line is most likely opposite to the direction of the electron beam firing. This supports the hypothesis that the waves are being driven by return currents and not directly by the beam.

In the shuttle rest frame the propagation velocity V of these waves is

$$V = -V_{sc} + V_g \tag{13}$$

where V_g is the group velocity of the waves in the plasma rest frame. For ion acoustic waves with a linear dispersion relation the group velocity is equal to the phase velocity. Considering that the shuttle and the PDP are moving at 7.4 km s^{-1} relative to the ionosphere, which is about 10 times the wave phase speed and group speed, it follows that ion acoustic waves would be convected over the PDP by the streaming motion of the ionospheric plasma. If the waves are generated along the magnetic field lines intersecting the shuttle, they will take of the order of 10^{-2} s to reach the PDP, which is much longer than the ion response time ($1/\omega_{pi}$), which is of the order of 10^{-4} s. If the ion acoustic speed is 1500 m s^{-1}, as indicated by equation (12), then the waves would have time to travel only about 15 m in the plasma rest frame. The PDP was about 93 m away from field lines intersecting the shuttle during the 0046–0047 UT event and about 170 m away during the 0247–0250 UT event. These estimates imply that the waves are generated within about 10 m of the magnetic field line through the shuttle. *Frank et al.* [1989], using measurements of the electron velocity distribution on the PDP spacecraft, reported that a magnetically aligned sheet of electrons was observed in the wake of the shuttle at 0411:13–0412:02 UT, returning from the direction of propagation of the electron beam. During this time period the PDP was about 15–45 m downstream from the magnetic field lines intersecting the shuttle. The thickness of this sheet of returning electrons was about 20 m. The hot returning electrons were also seen during the 0247–0250 UT event when the PDP was about 170 m downstream of the magnetic field lines intersecting the shuttle. Apparently the returning electron sheet still exists a few hundred meters downstream from the shuttle. Presumably, ion acoustic–like waves associated with the return current could be generated throughout this volume. However, it is reasonable to believe that the most intense part of the returning hot electron flux travels along the magnetic field lines intersecting the shuttle. It is very likely that the ion acoustic waves are most easily generated along these field lines and propagate at large angles with respect to the magnetic field line. The intersection point between V and B_{xz} is the most likely position for the ion acoustic waves to be generated in the X-Z plane. If the above argument is correct, during the 0046–0047 UT event the source of the observed waves was very close to the electron gun. The relevant geometry is shown in Figure 10. In this case the waves were propagating downstream. During the 0247–0250 UT event the source was about 100 m away from the shuttle. The relevant geometry for this case is shown in Figure 11. In the shuttle rest frame the waves were traveling upstream, indicating that the Doppler shift term was bigger than the measured frequency. The rest frame frequency was therefore negative. In both cases the observed wave vector directions were consistent with the waves being driven by the return current electrons, and not directly by the beam electrons.

Although ion acoustic–like waves can be generated over a large range of positions along the magnetic field lines inter-

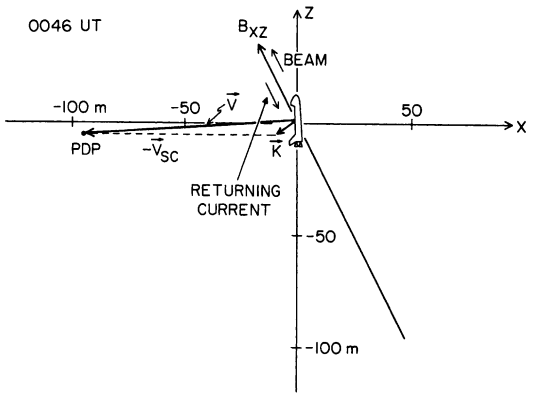

Fig. 10. The PDP and the wave source position of the 0046–0047 UT event in the X-Z plane.

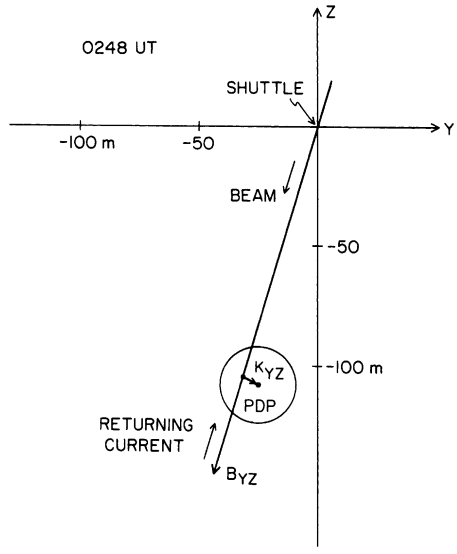

Fig. 12. The PDP and the wave source position of the 0247–0250 UT event in the Y-Z plane. The circle is the wave-generating circle, and the wave generated can be observed by the PDP.

secting the shuttle, the waves observed by the PDP spacecraft were generated in a very localized area along the magnetic field lines. This is because the waves were primarily convected over the PDP by the ionospheric plasma flow ($V_g \ll V_{sc}$). Since the background plasma flow was along the negative X axis, the wave generation region was near the intersection point between V_{sc} and B_{xz}. Using equation (13), it can be shown that the observed waves must originate in a circle in the Y-Z plane, centered on the intersection point as shown in Figure 12. Waves generated outside the circle cannot reach the PDP. The radius of the circle is about 10 m for the 0046 UT event and about 18 m for 0248 UT event. In both cases the magnetic field lines threading the shuttle intersect the circles as expected. Waves generated at different positions inside that circle must have differently directed wave vectors to reach the PDP. In other words, waves generated from each position within the circle have only one propagation angle that can be observed by the PDP. On the other hand, these ion acoustic waves are likely to be generated in a significant source volume and not just one single point position. If a broad angular range of ion acoustic waves was generated, the PDP should have simultaneously

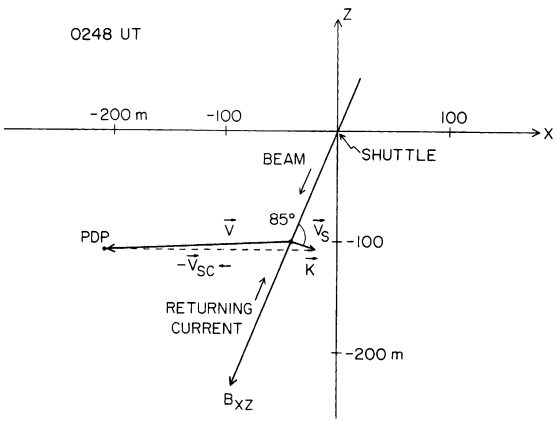

Fig. 11. The PDP and the wave source position of the 0247–0250 UT event in the X-Z plane.

observed waves with a broad distribution of wave vectors corresponding to the different positions inside the circle. However, we show next that the observations of well-defined "fingerprint" patterns during the 0046–0047 UT and 0248–0250 UT events argue that the waves came from a very concentrated range of angles. This means that the waves, whether or not they were observed by the PDP, all have highly oblique wave vectors with respect to the magnetic field.

In order to determine the allowed range of wave angles that can result in a well-defined interference pattern, a numerical simulation of interference patterns was compared to the real spectrum. This simulation is shown in Figure 13. Here we assume that the wave angular distribution has a Gaussian form with a standard deviation varying from 1° to 10°. These theoretical patterns are consistent with equation (10), assuming that the real power density $E_0^2(k_{xz})/\Delta f$ is a constant and summing over hundreds of wave angles α_k. By comparing the numerical simulation with the real interference patterns, we conclude that the range of wave-propagating angles (two standard deviations) is less than 10°.

On the other hand, if the waves are driven by the current returning along the magnetic field lines intersecting the shuttle, oblique ion acoustic waves should presumably be generated (and propagate) symmetrically with the same angle around the magnetic field line. Projecting this cone of wave vectors onto the X-Z plane, there should be two symmetric solutions, since the wave vector $\mathbf{k}_{xz}$ can point symmetrically on both sides of the magnetic field $\mathbf{B}_{xz}$ when $\mathbf{k}$ is almost perpendicular to $\mathbf{B}$. However, only one dominant angle is observed during both the 0046–0047 UT and 0248–0250 UT events. This asymmetry in the wave vector distribution is difficult to explain. Each wave propagation angle corresponds to a different source position. Although the other allowed source position on the same magnetic field line is within the wave-generating circle in the Y-Z plane for both

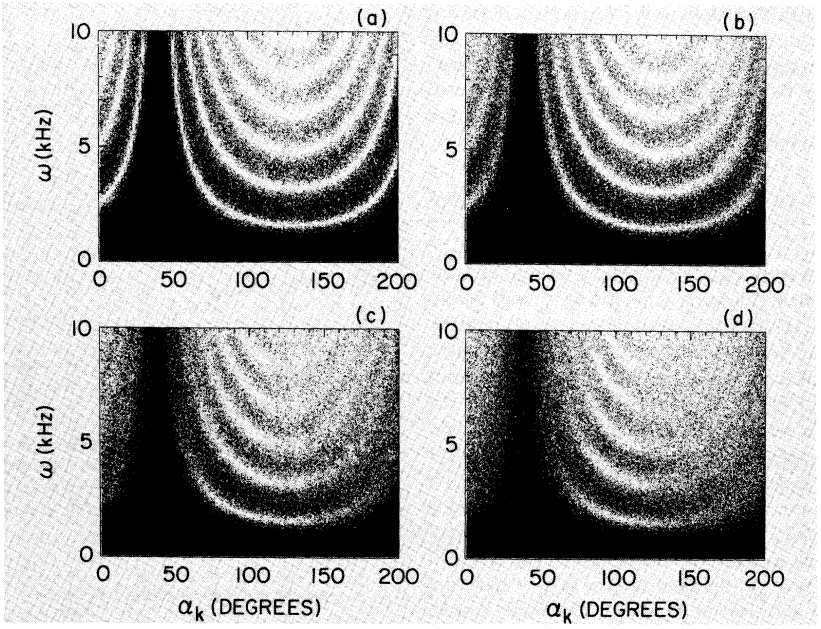

Fig. 13. The theoretical interference patterns with a Gaussian form wave angular distribution, assuming the range of wave-propagating angles θ is two standard deviations: (*a*) $\theta = 0°$, (*b*) $\theta = 5°$, (*c*) $\theta = 10°$, and (*d*) $\theta = 15°$.

events, it is farther away from the shuttle than the observed source position. Our best explanation of the asymmetric distribution of wave normal directions is that the strongest waves are generated when the shuttle is closest to the magnetic field line through the source.

6. Discussion

The FPEG events at 0119–0120, 0330–0337, and 0411–0418 UT have different characteristics than the 0046–0047 and 0248–0250 UT events. We do not observe a fingerprint pattern in the 0330–0337 UT event, although strong low-frequency waves are visible in the Helios spectrum analyzer data. During this period the PDP was near magnetic conjunction (at 0334 UT) with the shuttle from downstream. The waves in the low-frequency range were also most likely electromagnetic, since they were observed in both the electric and magnetic wideband data. Electromagnetic whistler mode radiation has been previously reported during this event [*Gurnett et al.*, 1986; *Farrell et al.*, 1988]. No low-frequency beam-generated electrostatic waves could be identified in the wideband data during this period. When the PDP was upstream from the shuttle (0334–0337 UT), the waves were carried away from the PDP by the background plasma (since $V_g \ll V_{sc}$) and did not have a chance to reach the PDP, which was upstream from the shuttle. When the PDP was downstream from the shuttle (0330–0333 UT), the PDP's Y position changed rapidly. The 0- to 10-kHz electric field spectrum was last measured at 0332:20–0332:46 UT prior to the magnetic conjunction. At that time the PDP was still more than 30 m away from the magnetic field lines intersecting the shuttle in the Y-Z plane, which means it was out of the returning current sheet region, so that the ion acoustic–like waves associated with the returning current could not be observed at 0330–0333 UT. During the 0411–0418 UT event the PDP was on the downstream side of the shuttle (after the magnetic connection with the shuttle). A poorly resolved interference pattern was observed in the 0- to 10-kHz wideband data during 0411:38–0412:04 UT. Although this pattern is not clear, it is similar to those observed during the 0046–0047 and 0248–0250 UT events. The wave vectors were also near perpendicular to the magnetic field. This means that the waves were also oblique ion acoustic–like waves but with a much broader range of propagation angles than the first two cases at 0046–0047 and 0248–0250 UT. During this time period the PDP was close to the magnetic field line intersecting the shuttle, and a current sheet of hot returning electrons was observed by *Frank et al.* [1989]. The PDP was therefore either inside or very close to the source region of the waves. The waves were received by the PDP almost immediately after they were generated. It is therefore reasonable that waves with a broad range of propagation angles should have been observed during this period. The poorly resolved interference pattern may also be due to the fact that the PDP simultaneously received waves that were directed both upstream and downstream. After the magnetic conjunction the PDP rapidly moved backward toward the original X-Z plane. The PDP was out of the wave-generating circle in the Y-Z plane after 0412 UT, so that the ion acoustic–like waves were observed only during the period 0411–0412 UT after magnetic conjunction. No ion acoustic–like waves were observed during 0413–0418 UT for the same reason that none were observed during the 0330–0333 UT event. The explanation for the 0119–0120 UT case is more difficult, because the PDP was in the wake region, about 90 m downstream from the shuttle. Apparently the ion acoustic–like waves generated along the magnetic field lines intersecting the FPEG were observed by the PDP over a broad range of wave normal angles during this time period.

The position of the PDP relative to the shuttle was close but also slightly different than for the 0046–0047 UT event. Other low-frequency electrostatic emissions were also observed before and during the electron gun firing. The expected interference patterns may have been obscured by these other electrostatic emissions.

ELF and VLF oscillations were also observed close to the shuttle during the electron beam emissions of the space experiments with particle accelerators (SEPAC) flown on the Spacelab 1 mission [*Neubert et al.*, *Cai et al.*, 1987]. The ELF oscillations were found in the return current and the potential measurement, indicating that the spacecraft potential and the ambient return currently oscillate at these frequencies. *Neubert et al.* [1986] found good evidence that these low-frequency oscillations are most likely caused by a drift wave instability driven by density gradients in the shuttle potential sheath. However, the electrostatic waves discussed in this paper are probably not drift waves. In the 0247–0250 UT event the waves are generated in a small region (Figure 12) which is located more than 100 m away from the shuttle along the magnetic field line. It is unlikely that the shuttle potential sheath would persist to such distances. In addition, the drift wave instability results in an electric field power spectrum proportional to k^{-3} [*Neubert et al.*, 1986]. This is not consistent with our deduced power spectrum in Figure 9.

Since the wave vectors are almost perpendicular (~85°) to the magnetic field and ion acoustic waves usually propagate at smaller angles to the magnetic field, the question arises, could these be ion cyclotron waves? (*Cai et al.* [1987] have suggested that the low-frequency fluctuations in the immediate vicinity of the shuttle are due to electrostatic ion cyclotron waves.) The O^+ cyclotron frequency was about 30 Hz. Our measured wave frequencies in the plasma rest frame are up to 600 Hz, which is within the higher order of the O^+ cyclotron harmonics region. We cannot rule out the possibility that the waves are high-order ion cyclotron waves, for two reasons. First, our frequency resolution is comparable to the ion cyclotron frequency. Second and more important, since the Doppler shift is the dominant term, even a small spread in the wave vector direction could blur the harmonics together.

To investigate this issue, we have used linear theory to study the characteristics of low-frequency electrostatic waves in a homogeneous, collisionless Vlasov plasma with characteristics similar to those believed relevant to the FPEG injection events. The plasma is assumed to have three components: background O^+ ions with a Maxwellian distribution, beam electrons modeled either as a Maxwellian beam or as a drifting ring distribution, and Maxwellian background electrons carrying a return current through a net drift along the magnetic field. The following plasma parameters were used: $n_O = n_{O^+} = 2 \times 10^4$ cm^{-3}, $n_b/n_O = 0.1$–0.5, $T_e = 2000$ K, $T_{O^+} = 1000$ K, $E_b = 1$ keV, $V_b = 75V_{te}$, and $\omega_{PO^+}/\omega_{ci} = 200$. Here the subscripts e, O^+, and b refer to the background electrons, O^+ ions, and FPEG beam electrons, respectively. The electrostatic dispersion equation is then of the form

$$1 + K_{O^+} + K_e + K_b = 0 \tag{14}$$

with

$$K_i = \frac{k_i^2}{k^2}\left\{1 + \sum_{-\infty}^{+\infty} \exp(-\lambda_i) I_m(\lambda_i) Z(\zeta_i^m)\left[\zeta_i^0 + \frac{m\Omega_i}{2^{1/2}k_\parallel v_i}\right]\right\}$$

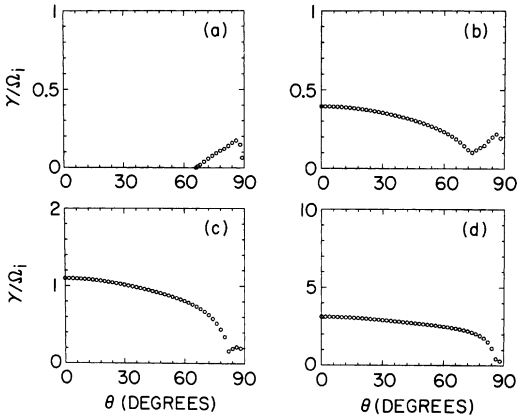

Fig. 14. Maximum wave rates as a function of wave propagation angles relative to the magnetic field. The panels correspond to different drift speeds V_e of ambient electrons: (*a*) $V_e/V_{te} = 0.60$, (*b*) $V_e/V_{te} = 0.72$, (*c*) $V_e/V_{te} = 0.80$, and (*d*) $V_e/V_{te} = 1.0$.

for a magnetized Maxwellian species i with equal parallel and perpendicular temperatures. Here $I_m(\lambda_i)$ denotes the mth-order modified Bessel of the second kind, $\lambda_i = k_\perp^2 V_i^2/\Omega_i^2$, and $Z(\zeta_i^m)$ denotes the Fried-Conte function with argument $\zeta_i^m = (\omega - k_\parallel v_\parallel - m\Omega_i)/2^{1/2} k_\parallel v_i$.

The dispersion relation given by equation (14) was solved for magnetized plasma conditions. When the drift speed for the ambient electrons carrying the return current is small ($0.3V_{te}$–$0.7V_{te}$), lower-order ion cyclotron harmonic waves become unstable while ion acoustic waves remain damped (Figure 14*a*). When the ambient electron drift speed increases above $0.7V_{te}$, ion acoustic waves first become unstable parallel to the magnetic field. The ion acoustic mode becomes unstable at increasingly oblique wave vectors as the drift speed increases, reaching the angles characteristic of ion cyclotron waves (85°–88°) when the ambient electron drift speed reaches $0.8V_{te}$–$1.0V_{te}$ (Figures 14*b*–14*d*). The growth rate of ion cyclotron waves is smaller than the growth rate of ion acoustic waves after the latter are generated. In addition, the maximum growth rate of the ion acoustic waves occurs for propagation parallel to the magnetic field. However, for the wave numbers observed in the fingerprint patterns, the growth rates are slightly larger at highly oblique angles than at small angles relative to the magnetic field. By comparing the growth rate with the measured power spectrum, it follows that the electron drift speed must be around V_{te}, where the ion cyclotron modes are mixed with the ion acoustic mode at very large angles. This drift speed is consistent with the measurements and simulation done by *Frank et al.* [1989].

Figure 15 shows the dispersion relation and growth rate of waves with $\theta = 86.5°$ when $V_e = 1.0V_{te}$. The maximum growth regions of the ion cyclotron harmonic waves mimic the ion acoustic waves. The waves switch from the ion cyclotron harmonic mode to the ion acoustic mode as the wave vector increases. At the same wave vector the wave switches from the ion cyclotron harmonic mode to the ion acoustic mode as the drift speed increases. As pointed out by *Kindel and Kennel* [1971], the highly oblique ion acoustic mode threads through the harmonic structure of ion cyclo-

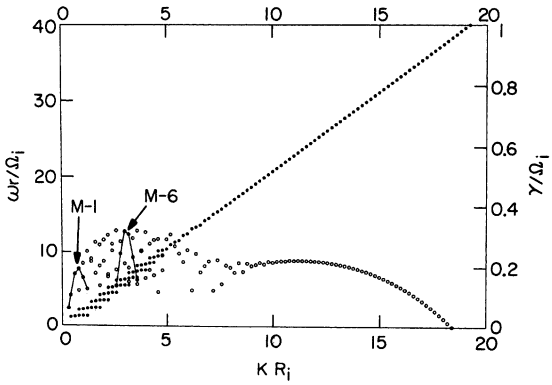

Fig. 15. Linear dispersion relation (solid circles) and growth rate (open circles) of the oblique ion acoustic–like waves with θ = 86.5° and $V_e = 1.0V_{te}$; the remnants of ion cyclotron–like structure are visible at small wave numbers. The order of the ion cyclotron harmonics is labeled by m.

tron modes. Therefore for highly oblique propagation, ion cyclotron harmonic waves are similar and nearly indistinguishable from ion acoustic waves. The linear theory also shows that the properties of the beam electrons do not have much effect on the ion acoustic waves, which prove that the waves are produced by the return current and ambient O^+ ions. In summary, we find that ion acoustic–like waves should have large growth rates over a wide range of propagation directions. Thus linear theory can explain the generation of highly oblique ion acoustic waves but cannot explain the restricted range of wave vector directions necessary to produce the observed interference patterns.

As discussed earlier, the measured phase speed for the waves is only about half the theoretical phase speed for unmagnetized ion acoustic waves. This discrepancy is addressed as follows. First, from the linear theory for magnetized electrons and oxygen ions we find that the phase speed of the unstable waves is lower than the unmagnetized ion acoustic speed for certain electron drift speeds. This decrease can be as large as 20%. Second, both the 0046–0047 UT and 0248–0250 UT events took place in darkness (nightside), in which case the electron temperature may be lower than the assumed value of 2000 K, which would further decrease the estimated ion acoustic speed.

The generation of ion acoustic waves by an electron beam has been predicted by various studies. Two mechanisms have been proposed. *Okuda and Ashour-Abdalla* [1988, 1990], *Okuda et al.* [1987], and *Pritchett* [1990, and references therein] have simulated electron beam injection into homogeneous plasmas. They find that a return flux of ambient electrons is required to balance the beam current. This return electron flux drifts relative to the background ions, so that ion acoustic waves can be generated by the return current. Using one-dimensional numerical simulations, *Okuda and Ashour-Abdalla* [1988] showed that ion acoustic waves propagating parallel to the magnetic field can be excited when the ambient electrons carrying the return current have a drift speed much less than the electron beam speed. *Hwang and Okuda* [1989] showed that oblique ion acoustic waves are generated when the drift speed of the return current electrons increased and was very large relative to the ion thermal speed. More detailed two- and three-dimensional simulations have been performed by *Okuda and Ashour-Abdalla* [1988, 1990] and *Pritchett* [1990, and references therein] and are limited to initial transient processes associated with the electron beam injection; these authors do not discuss the ion response.

The second mechanism was proposed by *Frank et al.* [1989]. On the basis of the Spacelab 2 data, they suggest that the ambient electrons in front of the beam electrons are forced to drift away from the shuttle due to the repulsive electric field at the front of the beam electrons. This drift of the background electrons relative to the ions drives ion acoustic waves by a two-stream instability. They also suggested that the ion acoustic waves provide a return flux of hot electrons by means of quasi-linear diffusion.

If the observed oblique ion acoustic waves are generated by a return current, then the component of the wave vector along the magnetic field should be the same as the drift direction of the ambient electrons. Accordingly, the wave vector directions obtained from the fingerprint patterns allow us to determine whether the observed ion acoustic waves are driven by a returning current of ambient electrons or by ambient electrons drifting away from the front of the beams as suggested by *Frank et al.* [1989]. Figures 10 and 11 demonstrate that the wave vectors observed in the 0046–0047 UT and 0247–0250 UT events are both consistent with a return current driving the observed waves by the ion acoustic instability and inconsistent with the mechanism proposed by *Frank et al.* [1989].

One major problem that presently remains unsolved is the identification of the exact wave mode, i.e., whether the waves are ion acoustic waves or high-order ion cyclotron harmonic waves. The ion acoustic mode experiences difficulties in explaining the observed severely restricted range of wave vectors directed at approximately 85° relative to the magnetic field. On the other hand, an interpretation involving ion cyclotron harmonic modes also encounters several problems. First, according to the linear theory, exciting the higher-order ion cyclotron harmonics modes ($m \geq 10$) requires a larger drift speed than for exciting the ion acoustic mode parallel to the magnetic field. After excited, the ion acoustic modes have larger growth rates than the ion cyclotron modes at very large angles to the magnetic field. Second, if the waves are pure ion cyclotron harmonics, then the group speed for each harmonic mode is near zero, which means that the waves are observed by the PDP at approximately the place they are generated. Both upstream and downstream waves should be observed by the PDP. However, the observation shows that the waves mostly propagate in one direction. In the 0046–0047 UT event it is clear that only downstream propagating electrostatic waves are presented in the wideband data. In the 0247–0250 UT event, although some evidence may suggest propagation in both directions, upstream waves should at least be more dominant than the downstream waves. Considering the idealized nature of the linear theory and the debatable assumptions of spatial homogeneity with a Maxwellian distribution for the return electrons, the inability of the linear theory to explain all aspects of the observations is not expected. Indeed, since the ion acoustic and ion cyclotron harmonic modes tend to have very similar dispersion relations and merge together for oblique propagation, it is very difficult to distinguish be-

tween these two wave modes. They are commonly viewed as the same wave mode.

On the basis of our analyses we believe that the beam-generated electrostatic waves detected by Spacelab 2 are highly oblique ion acoustic waves driven by return currents of ambient electrons. Accordingly, this work provides direct observational evidence that ion acoustic waves can be driven by injecting electron beams into a plasma, as has long been predicted on the basis of theory and simulations.

Acknowledgments. This research was supported by grant NAG3-449 from the NASA Lewis Research Center; grants NGL-001-043, NAGW-1539, and NAGW-2040 from NASA Headquarters; and contract NAS8-32807 with Marshall Space Flight Center.

The Editor thanks T. Neubert and another referee for their assistance in evaluating this paper.

REFERENCES

Buneman, O., Instability, turbulence, and conductivity in a current carrying plasma, *Phys. Rev. Lett.*, *1*, 8, 1958.

Bush, R. I., G. D. Reeves, P. M. Banks, T. Neubert, P. R. Williamson, W. J. Raitt, and D. A. Gurnett, Electromagnetic fields from pulsed electron beam experiment in space: Spacelab-2 results, *Geophys. Res. Lett.*, *14*, 1015, 1987.

Cai, D., T. Neubert, L. R. O. Storey, P. M. Banks, S. Sasaki, K. Abe, and J. L. Burch, ELF oscillations associated with electron beam injection from the space shuttle, *J. Geophys. Res.*, *92*, 12,451, 1987.

Farrell, W. M., D. A. Gurnett, P. M. Banks, R. I. Bush, and W. J. Raitt, An analysis of whistler mode radiation from the Spacelab 2 electron beam, *J. Geophys. Res.*, *93*, 153, 1988.

Frank, L. A., W. R. Paterson, M. Ashour-Abdalla, D. Schriver, W. S. Kurth, D. A. Gurnett, N. Omidi, P. M. Banks, R. I. Bush, and W. J. Raitt, Electron velocity distributions and plasma waves associated with the injection of an electron beam into the ionosphere. *J. Geophys. Res.*, *94*, 6995, 1989.

Fuselier, S. A., and D. A. Gurnett, Short wavelength ion waves upstream of the Earth's bow shock, *J. Geophys. Res.*, *89*, 91, 1984.

Gallagher, D. L., Short-wavelength electrostatic waves in the Earth's magnetosheath, *J. Geophys. Res.*, *90*, 1435, 1985.

Gurnett, D. A., W. S. Kurth, J. T. Steinberg, P. M. Banks, R. I. Bush, and W. J. Raitt, Whistler-mode radiation from the Spacelab 2 electron beam, *Geophys. Res. Lett.*, *13*, 225, 1986.

Gurnett, D. A., W. S. Kurth, J. T. Steinberg, and S. D. Shawhan, Plasma wave turbulence around the shuttle: Results from the Spacelab 2 flight, *Geophys. Res. Lett.*, *15*, 760, 1988.

Hwang, Y. S., and H. Okuda, Low-frequency electrostatic instabilities excited by injections of an electron beam in space, *J. Geophys. Res.*, *94*, 10,103, 1989.

Kindel, J. M., and C. F. Kennel, Topside current instabilities, *J. Geophys. Res.*, *76*, 3055, 1971.

Murphy, G. B., D. L. Reasoner, A. Tribble, N. D'Angelo, J. S. Pickett, and W. S. Kurth, The plasma wake of the shuttle orbiter, *J. Geophys. Res.*, *94*, 6866, 1989.

Narcisi, R., E. Trzcinski, G. Federico, L. Wlodyka, and D. Delorey, The gaseous and plasma environment around the space shuttle, *AIAA Pap. 83-2659*, 1983.

Neubert, T., et al., Waves generated during electron beam emissions from the space shuttle, *J. Geophys. Res.*, *91*, 11,321, 1986.

Okuda, H., and M. Ashour-Abdalla, Ion acoustic instabilities excited by injection of an electron beam in space, *J. Geophys. Res.*, *93*, 2011, 1988.

Okuda, H., and M. Ashour-Abdalla, Propagation of a nonrelativistic electron beam in three dimensions, *J. Geophys. Res.*, *95*, 2389, 1990.

Okuda, H., R. Horton, and M. Ono, Propagation of a nonrelativistic electron beam in a plasma in a magnetic field, *Phys. Fluids*, *30*, 200, 1987.

Paterson, W. R., and L. A. Frank, Hot ion plasmas from the cloud of neutral gases surrounding the space shuttle, *J. Geophys. Res.*, *94*, 3721, 1989.

Pickett, J. S., N. D'Angelo, and W. S. Kurth, Plasma density fluctuations observed during space shuttle orbiter water releases, *J. Geophys. Res.*, *94*, 12,081, 1989.

Pritchett, P. L., Spatial coherence during pulsed injection of electron beams, *J. Geophys. Res.*, *95*, 10,671, 1990.

Reasoner, D. L., S. D. Shawhan, and G. B. Murphy, Plasma Diagnostics Package measurements of ionospheric ions and shuttle-induced perturbations, *J. Geophys. Res.*, *91*, 13,463, 1986.

Reeves, G. D., P. M. Banks, T. Neubert, R. I. Bush, P. R. Williamson, A. C. Frazer-Smith, D. A. Gurnett, and W. J. Raitt, VLF emissions by pulsed and DC electron beams in space, 1, Spacelab 2 observations, *J. Geophys. Res.*, *93*, 14,699, 1988.

Reeves, G. D., P. M. Banks, T. Neubert, K. J. Harker, and D. A. Gurnett, VLF wave emissions by pulsed and DC electron beams in space, 2, Analysis of Spacelab 2 results, *J. Geophys. Res.*, *95*, 6505, 1990.

Shawhan, S. D., Description of the Plasma Diagnostics Package (PDP) for the OSS-1 shuttle mission and JSC chamber test in conjunction with the Fast Pulsed Electron Gun (FPEG), in *Artificial Particle Beams in Space Plasma Studies*, edited by B. Grandel, p. 419, Plenum, New York, 1982.

Shawhan, S. D., G. B. Murphy, and J. S. Pickett, Plasma Diagnostics Package initial assessment of the shuttle orbiter plasma environment, *J. Spacecr. Rockets*, *21*, 392, 1984.

Siskind, D. E., W. J. Raitt, P. M. Banks, and P. R. Williamson, Interactions between the orbiting space shuttle and the ionosphere, *Planet. Space Sci.*, *32*, 881, 1984.

Temerin, M., Doppler shift effects on double-probe measured electric field power spectra, *J. Geophys. Res.*, *84*, 5929, 1979.

Tribble, A. C., J. S. Pickett, N. D'Angelo, and G. B. Murphy, Plasma density, temperature, and turbulence in the wake of the shuttle orbiter, *Planet. Space Sci.*, *37*, 1001, 1989.

Winckler, J. R., The application of artificial electron beams to magnetospheric research, *Rev. Geophys.*, *18*, 659, 1980.

Winglee, R. M., and P. L. Pritchett, Comparative study of cross-field and field-aligned electron beams in active experiments, *J. Geophys. Res.*, *93*, 5823, 1988.

I. H. Cairns, W. Feng, and D. A. Gurnett, Department of Physics and Astronomy, University of Iowa, Iowa City, IA 52242.

(Received January 3, 1992;
revised April 6, 1992;
accepted April 15, 1992.)